

A modeling recipe to optimize the nanostructure excitonic Dye Sensitized Solar Cells (DSSCs)

M. AMERI^a, E. MOHAJERANI^b, F. SAMAVAT^a

^aDepartment of Physics, Bu- Ali Sina University, Hamedan, Iran

^bLaser and Plasma Research Institute, Shahid Beheshti University, Tehran, 1983969411, Iran

A numerical modeling recipe has been established to perform a parametric simulation on the transport properties of charged species in dye sensitized solar cells (DSSCs). The main outputs of the simulation are the charged species densities and current–voltage curve which determine the performance parameters of DSSC. But a realistic estimation of the performance parameters strongly depends on the number of physical parameters involved. To do so, we have attempted to engage the most recent theories in the present work. The results of the simulation allow the optimization of DSSC performance as a function of photoanode thickness. The highest power conversion efficiency belongs to the device with photoanode thickness of $20\mu\text{m}$. The model also highlights the importance of substrate/electrolyte interface in recombination of carriers. This model can be considered to be a tool to give a comprehensive view of DSSC operation in order to reduce the experimental workload aimed at optimizing DSSC performance.

(Received November 27, 2015; accepted February 10, 2017)

Keywords: Dye sensitized solar cell, Transport model, Current -voltage characteristics

1. Introduction

The dawn of dye-sensitized solar cell (DSSC) by Grätzel [1] opened a new pathway towards a high efficiency and low cost solar cell. Since then much research has focused on optimization of parameters for power generation in DSSCs [2-4]. The mechanism of power generation is a process whereby the dye on the nanocrystalline TiO_2 is excited by light, generating a fast electron transfer to the conduction band of the TiO_2 electrode and further movement toward the front electrodes. The oxidized dye is subsequently reduced by the electrolyte containing the iodide/tri-iodide redox couple, the formation of holes with movement toward the counter electrode through the electrolyte. Among nanoparticle oxide semiconductors, ZnO is assumed as a suitable alternative for TiO_2 [5]. Recently, power conversion efficiency of 12.3% is reported for dye sensitized solar cells [6].

Modeling this type of device to investigate the underlying factors controlling cell performance is an active area of research. Ameri et. al. [7] assumed diffusive currents to model the $J - V$ characteristics of nanoporous semiconductor films in DSSCs by taking electrolyte species transport into account. Salehi et. al. [8] investigated the transport of electrolyte ions to clarify its impact on the performance of the DSSC in the presence of flexible substrate. Ferber et. al. [9] developed a complete electrical model together with standard electrochemical chemistry to study internal cell properties. The model used drift-diffusion equations for all charged species in a system of pseudo-homogeneous TiO_2 layers intermixed with electrolyte active layers. They did not use a multi-trap

model (MTM) in their simulation. L. Peter [10] presented a complete simulation of DSSC response considering both trapping and no trapping separately in a continuity equation. The negligible effect of the electric field in the TiO_2 matrix was also discussed. Other work investigated the effect of bulk electrolyte thickness and electrolyte ion diffusion on the performance of DSSCs [11,12]. Anta et. al and Villanueva-Cab et. al. [13-15] proposed a continuity equation based on the MTM as well as a nonlinear recombination term to simulate the $J - V$ characteristics of the DSSC but they did not include electrolyte species transport in their model. Nithyanandam et. al. [16] proposed a model for analysis and design of DSSC. Ameri et. al. [17] performed a numerical simulation by considering continuity equations for electrons and electrolyte species considering the trapping and detrapping mechanism in DSSC; however, further optimization strategies for DSSCs are desirable.

The purpose of the present modeling recipe is to simulate the time and spatially dependent transport properties of the DSSC as well as its response by varying external and internal governing factors such as photoactive layer thickness, illumination direction and intensity, recombination constant, exchange current at the interface of the transparent conducting oxide (TCO), and electrolyte species diffusion coefficient. The findings of the present work are mainly based on simulated steady state $J - V$ characteristics which reveal some crucial performance parameters for further optimization of the cell. This modeling recipe has engaged most of the effective operation parameters of DSSC to predict the dynamic properties and provide a profound understanding and operation analysis of a manufactured cell. The novelty of this work lies in combining MTM, the quasi static

approximation (QSA) and nonlinear recombination of conduction band (CB) electrons with tri-iodide ions in the electrolyte to establish unsteady state continuity equations for electrons in the TiO_2 conduction band and iodide (I^-) tri-iodide (I_3^-) ions in the electrolyte solution. No previous model has incorporated MTM and all charged species, as we do, into transport equations to simulate the current-voltage characteristics of a DSSC. The effect of, illumination direction and intensity on short circuit current J_{SC} , open circuit voltage V_{OC} and electron diffusion length are presented. In addition, the optimum photoanode thickness for which the DSSC has a maximum power conversion efficiency (η) is calculated. Under open circuit condition there is almost no current flow through the TiO_2 /TCO interface. Therefore the TCO/electrolyte recombination current is the only current at the TiO_2 /TCO interface. The effect of this recombination current and TiO_2 CB electrons recombination on the $J - V$ curve are presented. The photoanode thickness dependence of electron diffusion length (L) is also investigated. The present method of DSSC analysis has the potential to determine optimization strategies to reduce the loss in the device.

2. Transport model

The DSSC generally consists of a pair of conducting glasses, a nanoporous TiO_2 layer covered by dye as the anode, the electrolyte and platinum coated conducting glass (TCO) as the cathode. Under illumination the dye is excited and injects an electron into the conduction band of TiO_2 . The transport of the injected electrons through the porous TiO_2 film to the TCO depends on the illumination intensity and the trapping–detrapping mechanism [18], (process 3 in Fig. 1). The oxidized dye molecules are regenerated by redox mediators, (I^- and I_3^-). Finally, for a complete DSSC operation cycle, the oxidized redox mediators I_3^- are transported to the counter electrode where they are regenerated. Due to the very small nanoparticle size (about 20nm) together with the strong screening effect of electrolyte, there is no significant macroscopic electric field in most of the porous thin film [19]. Therefore, both electrons and redox mediators are transported mainly by diffusion. The main electron loss reactions occurring in the DSSC are as the following: (i) direct dye relaxation to its ground state, (ii) capture of CB electrons by oxidized dye-molecules and (iii) recombination of CB electrons with tri-iodide ions in the electrolyte. (iv) recombination of trapped electrons in localized centers with tri-iodide ions in the electrolyte and (v) TCO/electrolyte electron recombination. Because of the slow rate of processes (i), (ii) and (iv) the only loss mechanisms which are taken into account are (iii) and (v) (processes 1 and 2 in Fig. (1)) [9].

The cell is assumed to have a thickness of d composed of an intermixed combination of the TiO_2 nanoporous layer, the dye and the redox electrolyte (Fig. 1). This system is sandwiched between two glass layers coated with a thin transparent conducting oxide.

The charged species are electrons in TiO_2 CB, iodide and tri-iodide ions in the electrolyte and positively charged cations.

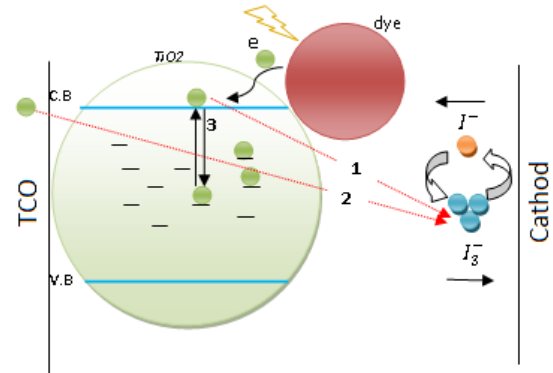


Fig. 1. The scheme of the model. DSSC operation and loss processes 1, 2 and trapping–detrapping mechanism (3) of C.B electrons. The electron transport occurs in the TiO_2 CB. Iodide and tri-iodides are transported in the electrolyte solution in opposite directions. The cell is illuminated from both working electrode (photoanode) and counter electrode (cathode)

Table 1. Input parameters relevant to simulation of current - voltage characteristics

Parameter	Value	Parameter	Value
n^0	$1 \times 10^{22} \text{m}^{-3}$ [9]	Φ_{inj}	1
n_{tri0}	$1 \times 10^{25} \text{m}^{-3}$ [11]	σ	0.5
n_{i0}	$1 \times 10^{26} \text{m}^{-3}$ [11]	p	0.5
D_{i0}	$6 \times 10^{-10} \text{m}^2 \text{s}^{-1}$ [11]	e	$1.602 \times 10^{-19} \text{C}$
D_{tri0}	$5 \times 10^{-10} \text{m}^2 \text{s}^{-1}$ [11]	k_b	$1.38 \times 10^{23} \text{m}^{-2} \text{kg} \text{s}^{-2} \text{K}^{-1}$
D_0	$3 \times 10^{-8} \text{m}^2 \text{s}^{-1}$ [9]	N_c	$1 \times 10^{21} \text{cm}^{-3}$

The proposed modeling recipe is as follows: First, the basic relations for nanocrystalline semiconductors are combined with QSA are adopted to derive a relation for electrons in the CB, n_c , and trapped electrons, n_t , in localized centers. Next, a continuity equation is constructed for all charged species using the above relation as well as electron generation and recombination terms. In the third step, the set of partial differential equations are solved imposing appropriate boundary and initial conditions to calculate time and spatial dependent electron, iodide and tri-iodide density profiles then the time and spatial current density is calculated using the electron density gradient. And finally, to produce the current-

voltage curve the voltage is varied from an open circuit to a short circuit condition repeating the above steps.

2.1. Electronic transport

The proposed model is based on well-known concepts for studying a nanocrystalline semiconductor. The first concept is that of a quasi-Fermi level (QFL) which states that when a semiconductor is under illumination, electrons are injected into the conduction band, raising the Fermi level and a density gradient is established. The second is multi-trap model (MTM) in which the electron transport is assumed to happen via extended states E_c [20,21]. However, the transport is slowed down by successive trapping and detrapping of electrons to and from localized trap centers. The result of this model is an effective diffusion coefficient and recombination constant that are quasi-Fermi level QFL (or electron density) dependent. The last concept is the QSA [21] which assumes that the trapping and detrapping processes are much faster than the transport and recombination processes.

In a semiconductor the density of states, D_e in the CB is the number of electron states per volume and per energy interval:

$$D_e(E_e) = \frac{1}{V} \frac{dN_e}{dE_e}$$

and the density of electron in CB

$$n = \int_{E_c}^{\infty} D_e(E_e) f(E_e) dE_e$$

where $f(E_e)$ is the Fermi-Dirac function. When the Fermi level is separated from the CB by more than $3KT$, where K is the Boltzmann constant,

$$f(E) \approx f_B(E) = \exp\left[\frac{-E_{f0}}{KT}\right]$$

If E_{f0} is the Fermi level with no illumination, then the CB electron density n_c^0 can be written

$$n_c^0 = N_c \exp\left[\frac{-E_{f0}}{KT}\right] \quad (1)$$

where $N_c = 2 \left(\frac{2\pi m_e^* KT}{h^2}\right)^{\frac{3}{2}}$ is the effective density of states in the CB, m_e^* is the electron effective mass and h is the Planck constant. According to the QFL approximation, under illumination electrons are injected to the CB and the Fermi level is raised, so

$$n_c(x) = N_c \exp\left(\frac{-E_f(x)}{KT}\right) \quad (2)$$

In a nanocrystalline semiconductor the trap energy distribution follows from

$$g(E_t) = \alpha \frac{N_t}{KT} \exp\left(\frac{-\alpha E_t}{KT}\right) \quad (3)$$

where N_t , α and T are the total trap density, trap parameters and temperature respectively.

Assume that most electrons are trapped ($n \approx n_t$) we can write:

$$n(x) = N_t \exp\left(\frac{-\alpha E_f}{KT}\right) \quad (4)$$

$$n^0 = N_t \exp\left(\frac{-\alpha E_{f0}}{KT}\right) \quad (5)$$

Combining eqs. (1, 2, 4 and 5) we arrive at:

$$KT \ln\left(\frac{n^0}{n(x)}\right) = \alpha \left(KT \ln\left(\frac{n_c^0}{n_c(x)}\right)\right) \quad (6)$$

where n and n_c are total and free electron densities. Finally, Eq. (6) yields

$$n_c = N_c \left(\frac{n_t}{N_t}\right)^{\frac{1}{\alpha}} \quad (7)$$

The continuity equations for electrons in the photoanode is

$$\frac{\partial n_c(x, t)}{\partial t} = \frac{\partial}{\partial x} D_0 \frac{\partial n_c(x, t)}{\partial x} + G_e(x, \lambda) - R_e(x, t) - \frac{\partial n_t(x, t)}{\partial t} \quad (8)$$

where D_0 is the diffusion coefficient and n_t , n_c are trapped and free electron densities. $G_e(x, \lambda)$ is the electron generation term for working electrode (WE) side illumination and is calculated applying the Beer-Lambert law for the absorption coefficient:

$$G_e(x, \lambda) = \int_{\lambda_{min}}^{\lambda_{max}} \phi_{inj} I_0(\lambda) abs(\lambda) \exp[-abs(\lambda) x] d\lambda \quad (9)$$

while for the counter electrode (CE) side illumination we have:

$$G_e(x, \lambda) = \int_{\lambda_{min}}^{\lambda_{max}} \phi_{inj} I_0(\lambda) abs(\lambda) \exp[-abs(\lambda)(d - x)] d\lambda \quad (10)$$

where ϕ_{inj} is the quantum injection yield, $I_0(\lambda)$ the solar irradiation spectrum for AM1.5 and $abs(\lambda)$ the absorption coefficient of the N719 dye^[22]. The interpolated functions, $abs(\lambda)$ and $I_0(\lambda)$, are inserted in $G_e(x, \lambda)$. After integration, a table of $G_e(x, \lambda)$ values for 100 spatial points is generated in Mathematica 9 and finally $G_e(x, \lambda)$ values

were interpolated to build a function to ease the computation process.

The charge reaction transfer between TiO_2 and redox electrolyte is a single electron reaction

$$I - \frac{k_f}{k_b} \rightleftharpoons I + e^-$$

in which k_f and k_b are forward and backward reaction rates. Applying a standard chemical approach, the reaction rates are proportional to concentrations of species involved. In the absence of illumination

$$k_f n_I = k_b n^0 n_{i0} \quad (11)$$

where n_I is the iodine (I) density - the oxidized species of the charge-transfer reaction. Eq. (11) implies that the forward reaction rate equals the backward reaction rate. Finally the net electron flow at the interface may be written as [9]

$$R_e = k_b n n_I - k_f n_i \quad (12)$$

Taking the mass action law into account and considering non-linear chemical kinetics, the recombination term can be rewritten as:

$$R_e(x, t) = k_0 \left\{ \begin{array}{l} (n_c(x, t))^\beta \sqrt{\frac{n_{tri}(x, t)}{n_i(x, t)}} \\ - n^0 \beta \sqrt{\frac{n_{tri0}}{(n_{i0})^3}} n_i(x, t) \end{array} \right\} \quad (13)$$

where k_0 and β are the recombination constant and the recombination reaction order respectively. Recently, Ansari et al [23] showed that β is less than or equal to unity. $n_c(x, t)$, $n_{tri}(x, t)$, $n_i(x, t)$, n^0 , n_{tri0} and n_{i0} are the electron densities in the CB, the tri-iodide density, the iodide density, the initial electron density in the CB, the initial tri-iodide density and the initial iodide density respectively. Making use of mathematical form of the QSA:

$$\frac{\partial n_c(x, t)}{\partial t} = \frac{\partial n_c(x, t)}{\partial n_t} \frac{\partial n_t(x, t)}{\partial t} \quad (14)$$

and using Eq. (7) and assuming that most electrons are trapped ($n \approx n_t$), one obtains:

$$\frac{\partial n_t}{\partial n_c} = \left(\frac{N_c}{\alpha N_t^{\frac{1}{\alpha}}} n^{\frac{1-\alpha}{\alpha}} \right)^{-1} \quad (15)$$

By rewriting Eq. (8) using the equation above, we reach the continuity equation corresponding to an electron density dependent diffusion coefficient and an electron density dependent recombination constant

$$\begin{aligned} & \left(1 + \frac{D(n)}{D_0} \right) \frac{\partial n(x, t)}{\partial t} \\ &= \frac{\partial}{\partial x} \left(D(n) \frac{\partial n(x, t)}{\partial x} \right) + G_e(x, \lambda) \\ & - \left\{ k(n) n(x, t) \sqrt{\frac{n_{tri}(x, t)}{n_i(x, t)}} \right. \\ & \left. - k_R (n^0)^\beta \sqrt{\frac{n_{tri0}}{(n_{i0})^3}} n_i(x, t) \right\} \\ & + \frac{dn_{tco}}{dx} \end{aligned} \quad (16)$$

With

$$\begin{aligned} D(n) &= D_0 \frac{\partial n_c}{\partial n_t} \quad (17) \\ k(n) &= k_R \frac{(N_c)^\beta}{\alpha N_t^{\frac{\beta}{\alpha}}} n^{\left(\frac{\beta}{\alpha}-1\right)} \end{aligned}$$

Finally the diffusive current is calculated at $x = 0$ by

$$J(x, t) = eD(n) \frac{dn(x, t)}{dx} \quad (18)$$

Here the contribution of drift in electron and ion transport is neglected. Due to a very short Debye length the electrical field is not significant [10, 19]. The main driving force for collecting electrons originates from electron density gradient in the vicinity of $x = 0$, ie the diffusion current has the only significant role in electron transport. The additional term, $\frac{dn_{tco}}{dx}$, on the right hand side of Eq. (16), is the recombination current from TCO to the electrolyte which can be calculated from Butler-Volmer equation

$$J_{tco} = J_{tco0} \left\{ \exp \left[\frac{-(1-\sigma)eV}{KT} \right] - \exp \left[\frac{\sigma eV}{KT} \right] \right\} \quad (19)$$

where J_{tco0} and σ are the exchange current density and cathodic electron transfer. It describes how the electrical current on an electrode depends on the electrode potential, considering that both a cathodic and an anodic reaction occur on the same electrode. It should be emphasized here that Eq. (19) is only valid in this simple form if the current is really kinetically controlled, i.e. if diffusion of the redox species toward the electrode surface is sufficiently fast [24].

2.2. Electrolyte species transport

The transport of the redox species has a great impact on DSSC performance. The generation of two electrons always gives rise to the generation of one tri-iodide ion and the loss of three iodide ions i.e.:

$$\begin{aligned} \frac{1}{2}(G_e(x, \lambda) - R_e(x, t)) &= (G_{tri}(x, \lambda) - R_{tri}(x, \lambda)) \\ &= -\frac{1}{3}(G_i(x, \lambda) - R_i(x, \lambda)) \end{aligned} \quad (20)$$

where $G_i(x, \lambda)$, $G_{tri}(x, \lambda)$, $R_i(x, \lambda)$, $R_{tri}(x, \lambda)$ are the iodide and tri-iodide generation and recombination rates, respectively. Therefore the continuity equations for mobile charged species in electrolyte are:

$$\begin{aligned} \frac{\partial n_i(x, t)}{\partial t} &= D_i \frac{\partial^2 n_i(x, t)}{\partial x^2} \\ -\frac{3}{2p}(G_e(x, \lambda) - R_e(x, t)) \end{aligned} \quad (21)$$

$$\begin{aligned} \frac{\partial n_{tri}(x, t)}{\partial t} &= D_{tri} \frac{\partial^2 n_{tri}(x, t)}{\partial x^2} \\ +\frac{1}{2p}(G_e(x, \lambda) - R_e(x, t)) \end{aligned} \quad (22)$$

where D_i , D_{tri} and p are the iodide and tri-iodide diffusion coefficients and the porosity of the photoanode.

The system of partial differential equations, 16, 21 and 22, can be solved simultaneously by applying appropriate initial and boundary conditions (BC) for the electrons and iodide and tri-iodide species as follows

$$\begin{aligned} n(0, t) &= n(x, 0) = n^0 \exp\left(\frac{\alpha eV}{KT}\right), \\ \frac{dn(d, t)}{dx} &= 0 \end{aligned} \quad (23)$$

The first BC indicates that the initial electron density at the beginning of photoanode is voltage dependent and the second assures zero current density at the end of photoanode.

$$\begin{aligned} \frac{\partial n_i(0, t)}{\partial x} &= -\frac{3J_{tco}}{2eD_i}, \\ \int_0^d n_i(x, t) dx &= n_{i0}pd, n_i(x, 0) = n_{i0} \end{aligned} \quad (24)$$

$$\begin{aligned} \frac{\partial n_{tri}(0, t)}{\partial x} &= \frac{1J_{tco}}{2eD_{tri}}, \\ \int_0^d n_{tri}(x, t) dx &= n_{tri0}pd, n_{tri}(x, 0) = n_{tri0} \end{aligned} \quad (25)$$

The first two BCs in eqns. (24) and (25) show that the electrolyte ion current at the beginning of photoanode is associated with the TCO/electrolyte back reaction. The second equations assures particle conservation through the photoanode thickness.

The simulation code is written in Mathematica 9 applying the *Method of Lines and NDSolve* command to solve the set of partial differential equations. This explicit numerical method replaces all spatial derivatives with finite differences but does not alter the time derivatives. It is then possible to use a stiff ordinary differential equation solver on the time derivatives in the resulting system.

The incident photon-to-current conversion efficiency (*IPCE*) is defined as the ratio of the number of electrons generated by the solar cell to the number of photons of a given energy incident on the solar cell:

$$IPCE = \frac{en}{en_{ph}} = \frac{J_{sc}}{en_{ph}} \quad (26)$$

where n_{ph} and J_{sc} are number of incident photons and short circuit current, respectively. The power conversion efficiency of a solar cell is determined as the fraction of incident power which is converted to electricity and is defined as:

$$\eta = \frac{P_{MP}}{P_{in}} \quad (27)$$

where $P_{MP} = V_{OC} J_{SC} FF$ and V_{OC} , J_{SC} , FF and P_{in} are the short-circuit current, open-circuit voltage, the fill factor and input power respectively.

3. Results and discussion

The behavior of the electron density profile under different operation conditions plays the most important role in determining all transport properties. Fig. 3(a) shows the time and spatial dependent behavior of electron density profile under short circuit conditions in the photoactive layer under WE side illumination. At each spatial point, the electron density profile increases with time and reaches an almost constant value. The electron density increases by reaching deeper into the photoanode. It is clearly seen that the electron density gradient is much larger at points close to $x = 0$. It implies that the first micrometers of photoanode, where most electrons are generated (Fig. 2), mainly contributes to total current density. Fig. 3 (b) shows the time and spatial dependent electron density profile under CE side illumination. The electron density reaches higher values through the photoanode in comparison with WE side illumination. By increasing the incident light intensity, the electron density gradient near $x = 0$ increases, so that a larger short circuit current density is obtained (Fig. 3 c). As x increases, the electron density increases but its gradient decreases.

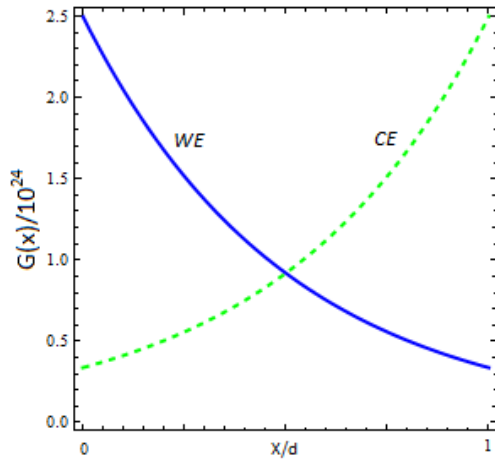


Fig. 2. Electron generation rate, $G(x, \lambda)$, under WE and CE side illumination through photoanode thickness, Under a standard 1Sun and AM1.5 condition. Film thickness $d = 20\mu\text{m}$

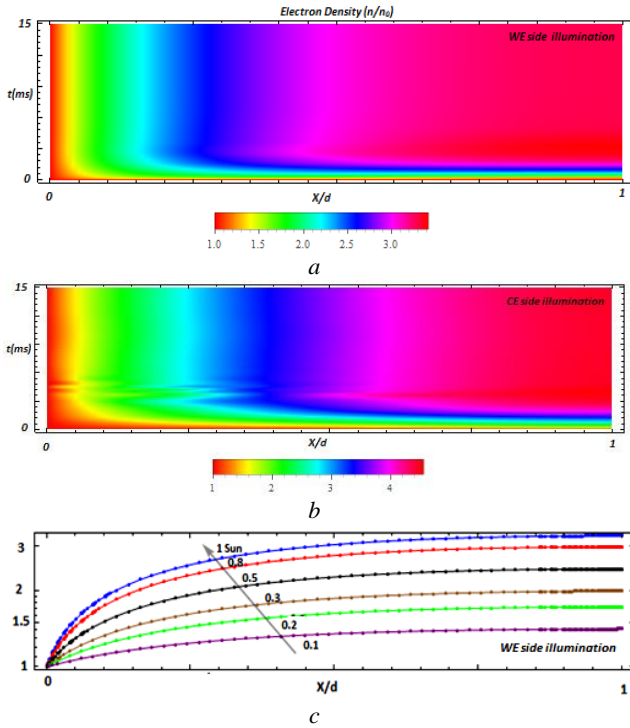


Fig. 3. Time and spatially dependent electron density profiles under WE side illumination (a) and CE side illumination (b) under SC conditions. The electron density profile in the photoactive layer under SC for different illumination intensities under WE side illumination (c). Film thickness is $d = 20\mu\text{m}$

Charged carriers in the electrolyte play a crucial role in the optimized design of a DSSC. Figs. 4 a-d show the time and spatial dependence behavior of electrolyte species density profiles under short circuit (SC) and open circuit (OC) conditions.

As expected, under SC condition the iodide density decreases at spatial points close to $x = 0$ and increases at points closer to the counter electrode where they are mainly generated, Fig. 4(a). However the iodide density is higher under the OC circuit condition (Fig. 4 b). This is due to recombination process in which iodide could also be formed. The tri-iodide density increases in the vicinity of the working electrode and decreases towards counter electrode due to recombination with free and trapped electrons. Under both SC and OC conditions the gradient of tri-iodide density profile increases at points closer to $x = 0$ as time passes (Fig. 4 c and d).

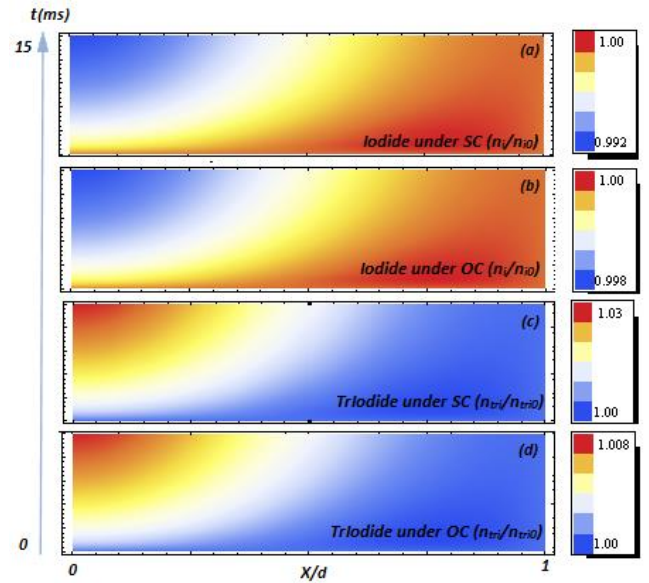


Fig. 4. Time and spatially dependent iodide density profiles under SC (a) and OC conditions (b). Time and spatially dependent tri-iodide density profiles under SC (c) and OC conditions (d) under WE side illumination. The films thickness is $d = 20\mu\text{m}$. The densities are expressed as reduced values $(\frac{n_i(x,t)}{n_{i0}}, \frac{n_{tri}(x,t)}{n_{tri0}})$

Fig. (5) shows the variations of the electrolyte species densities with respect to their diffusion coefficients. The decrease in tri-iodide diffusion coefficient leads to an increase in tri-iodide density in vicinity of $x = 0$. This is due to slower transport of the tri-iodide species towards the counter electrode which causes the accumulation of the tri-iodide species close to $x = 0$. On the other hand, the iodide density decreases at points close to $x = 0$ and $x = d$ by decreasing the diffusion coefficient which leads to accumulation of the iodide species in regions close to $x = d$ and leads to slower transport of the species towards the anode. Faster electrolyte ion transport can enhance dye regeneration, leading to more efficient electron injection into the TiO_2 CB.

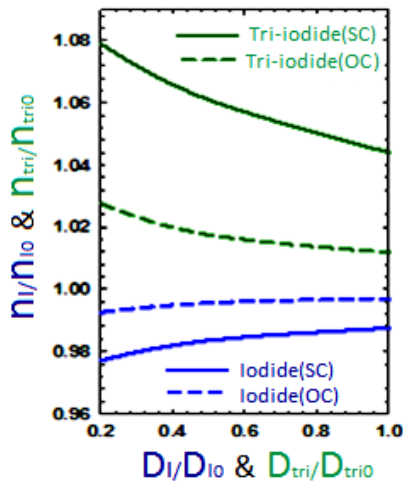


Fig. 5. Iodide and tri-iodide density versus diffusion coefficient under SC and OC conditions for a film thickness $d = 20\mu\text{m}$

By increasing the incident light intensity, the tri-iodide density and gradient increases close to $x = 0$ where the highest current density is obtained (Fig. 6 a). The latter reflects the fact that for higher SC current densities we need faster tri-iodide transport from the anode to cathode. It can be seen that at low light intensities the tri-iodide density decreases in the vicinity of the TCO, so the back reaction between the TCO/electrolyte can be reduced resulting in less OC voltage loss. On the other hand, the iodide density and gradient increases close to $x = d$, where the iodide species is generated (Fig. 6 b). By increasing the light intensity the gradient of the iodide at $x = d$ is increased resulting in more efficient iodide transport from cathode to anode.

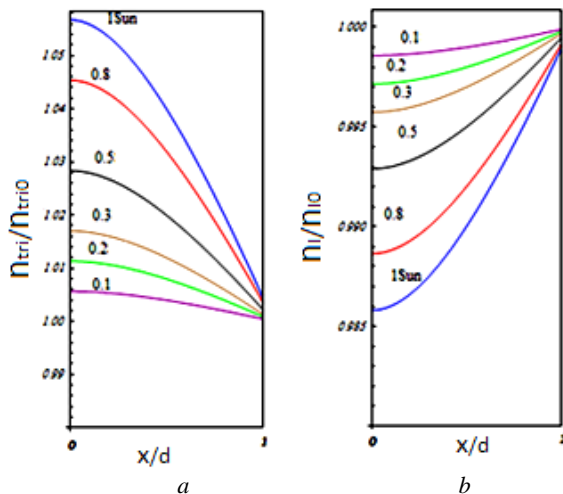


Fig. 6. Iodide (a) and tri-iodide (b) density profiles in the photoanode under SC conditions for different illumination intensities with WE side illumination and a film thickness $d = 20\mu\text{m}$

The steady-state $J - V$ characteristics gives the performance parameters of the cell, such as the short-circuit current (J_{SC}), open-circuit potential (V_{OC}) and fill

factor (FF). Nevertheless, more detailed properties cannot be extracted from steady-state measurements. Fig.7(a) represents the illuminated $J - V$ characteristics of the DSSCs simulated under a AM1.5 spectrum for film thicknesses from $5 - 20\mu\text{m}$ with WE side illumination. For model validation, the calculated $J - V$ curve for $d = 10\mu\text{m}$ is compared with experimental values [9]. Fig. 7(b) shows the variations of J_{SC} with respect to film thickness for different incident light intensities. The J_{SC} increase is a result of IPCE improvement as shown in Fig. 11(d) implying uniform charge generation throughout the film [25]. In addition, the improvement of J_{SC} is related to the increase in injecton current from the excited dyes to the CB of TiO_2 arising from the increased surface area and more dye adsorption. Another reason for the J_{SC} increase can be related to the V_{OC} drop as can be seen in Fig. 7(c). The V_{OC} decrease means that the CB edge of TiO_2 shifts positively. The positive shift with respect to dye energy narrows the energy difference between TiO_2 and the dye which allows low lying excited states of the dye to inject electrons, leading to a rise in J_{SC} [26, 27]. The decrease in V_{OC} by varying the thickness can be related to back electron transfer to tri-iodide ions. Increasing the surface area of the electrode as a result of increasing film thickness leads to an increase in surface trapping states which can cause back electron transfer. The effect of light intensity is shown in Fig. 8(b).

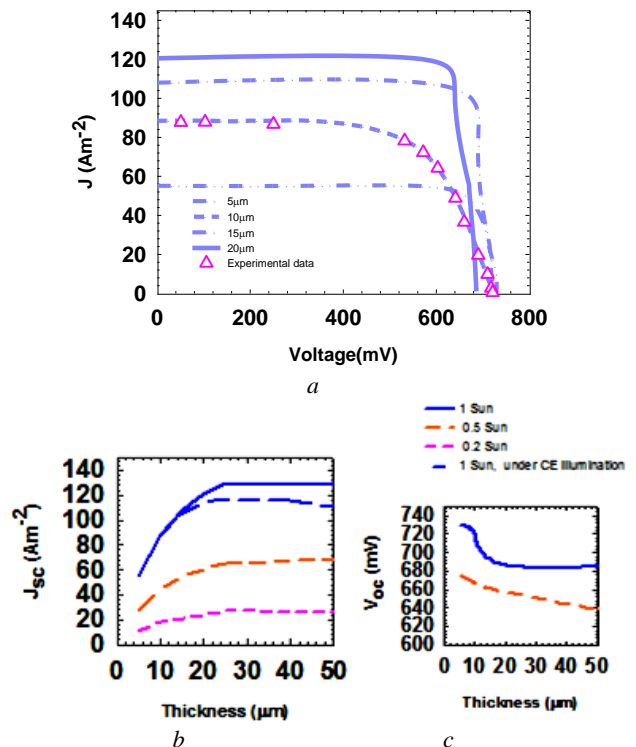


Fig. 7. The $J - V$ characteristics of the DSSC under WE side illumination for different film thicknesses. The model is compared with experimental data [9] for model validation (a). The calculated J_{SC} of the DSSC under WE and CE side illumination versus film thickness for different light intensities (b). The V_{OC} of the DSSC under WE side illumination versus film thickness for different light intensities (c)

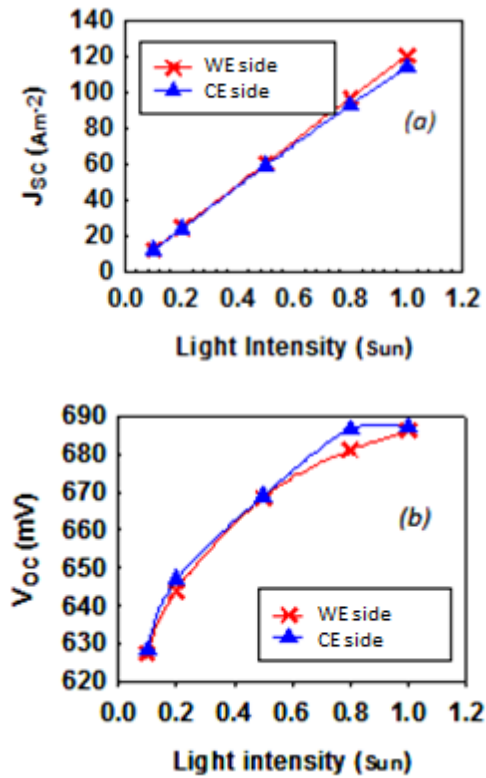


Fig. 8. The variations of J_{sc} (a) and V_{oc} (b) versus illumination intensity under WE and CE side illumination for film thickness of $d = 20\mu m$

The calculated variations of J_{sc} and V_{oc} with respect to incident light intensity for WE and CE side illumination and a film thickness of $d = 20\mu m$ are shown in Figs. 8(a) and (b) at light intensities around 0.7-1 Sun. J_{sc} for WE side illumination becomes larger in comparison to CE side illumination while for V_{oc} it is the opposite. This result can be assigned to an increase in the injected charge flux leading to a higher V_{oc} which is consistent with the relationship $V_{oc} = (kT/e) \ln(I_{inj}/R)$, where I_{inj} is the charge flux from the excited dye and R is the rate of the back electron recombination[28].

The effect of varying the recombination constant on the $J - V$ characteristics is shown in Fig. 9(a). The immediate effect of increasing the recombination constant is the decrease in V_{oc} . The lower K_{R0} , i.e. the lower rate of the electron recombination, the higher the electron concentration in the TiO_2 CB. A higher electron concentration means a higher quasi-Fermi level E_f and thus a higher voltage.

Another important interfacial recombination process is TCO/electrolyte recombination current J_{tco} which leads to OC voltage loss. Fig. 9(b) shows the effect of the latter on the current-voltage curve calculated without applying external series and parallel resistances. It is clear that increasing J_{tco0} values have a considerable effect on the FF.

Carrier diffusion length (L) is the average distance a carrier can move from the point of generation until it recombines. Determining L in DSSCs has been the subject

of many recent studies [29,30]. The values of electron diffusion coefficient and electron lifetime can be used to calculate the electron diffusion length, $L = (D\tau)^{1/2}$. Here it is calculated by assuming $L = (D(n)/k(n))^{1/2}$.

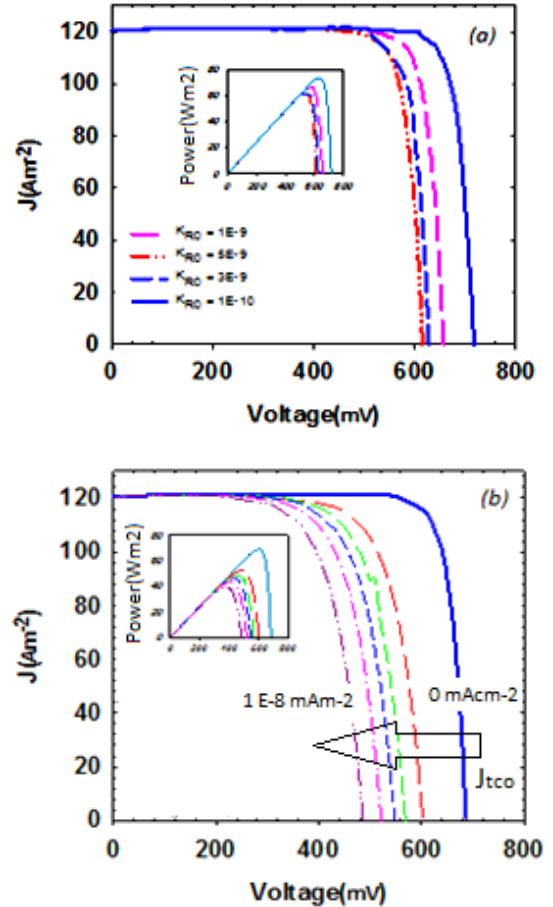


Fig. 9. The effect of varying the recombination constant (a) and exchange current values (b) on the $J - V$ curves and the output power versus V (inset)

In experiment the transport and interfacial transfer of electrons in dye-sensitized solar cells are measured using intensity modulated photocurrent and photovoltage spectroscopy (IMPS and IMVS respectively). IMPS provides information about the dynamics of charge transport and back reaction under SC conditions, whereas the IMVS response is determined by the electron lifetime under OC conditions [31]. Interpretation of the behavior of the diffusion length is ambiguous from a fundamental point of view. The result of our calculations indicates that L shows a weak dependence on light intensity due to the compensation for the decrease in the carrier life time and the increase in diffusion length [32]. The result of calculations for the thickness dependence of L under SC is shown in Fig. 10(a). Higher values of L for thicknesses less than $d = 20\mu m$ are obtained. For thicker films, the electron diffusion is more difficult and large number of photogenerated electrons recombine without reaching the front electrode leading to a decrease in L . Fig. 10(b) shows

the variation of L throughout the film under SC, the maximum power point (MP) and OC for both WE and CE side illumination. Under OC the diffusion lengths for both illumination sides almost overlap are higher than diffusion lengths for SC and MP conditions throughout the photoanode.

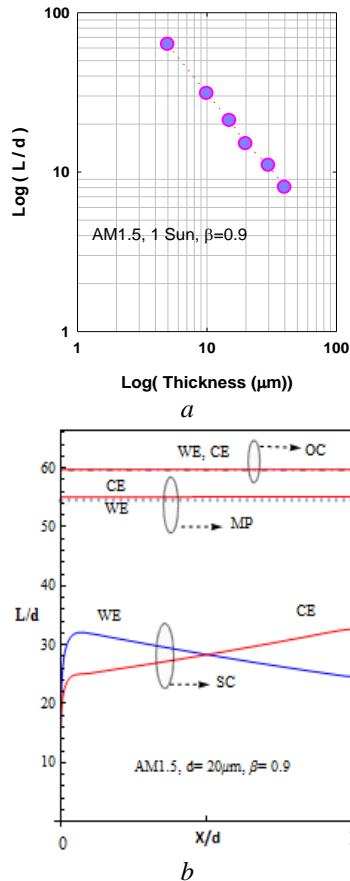


Fig. 10. The effect of nonlinear recombination. The variation of diffusion length versus film thickness (a) The diffusion length versus distance, x , from the anode for film thickness of $20 \mu\text{m}$ under SC, MP and OC (b)

The overall performance of the DSSC can be evaluated in terms of cell efficiency and fill factor. The simulated performance parameters of DSSC vs. film thickness and light intensity are shown in Fig.11 (a-d). The FF , which indicates the squareness of the $J-V$ curve, and internal resistance of the device are shown in Fig. 11(b). Except for an illumination intensity of 0.2 Sun, the diagrams show a maximum FF for a film thickness of about $15\text{-}20 \mu\text{m}$ which implies a decrease in cell internal resistance in this thickness interval. With a further increase in film thickness, a lower FF and higher internal resistance are obtained. Similar behavior for maximum power point is obtained (Fig. 11 a). η is a direct function of the already mentioned performance parameters. Thus, it is expected that the highest η to happen in the interval of $15\text{-}22 \mu\text{m}$ (Fig. 11 c). Our predicted optimum film thickness of about $20 \mu\text{m}$ interval is in straight agreement with experimental reports [33-37]. Fig. 11 (d) shows the simulated IPCE for different film thicknesses with varying light intensity. The

IPCE increases abruptly for thicknesses less than $20 \mu\text{m}$ and reaches almost the same value regardless of film thickness, since a change in film thickness has no effect on the photo process. The increase in $IPCE$ can be attributed to the enhancement of the electronic diffusion coefficient. However, J_{SC} enhancement with increasing thickness (Fig. 7b) is a direct consequence of the $IPCE$ improvement. There is also an increase in $IPCE$ with an increasing light intensity which also agrees well with experimental reports [38].

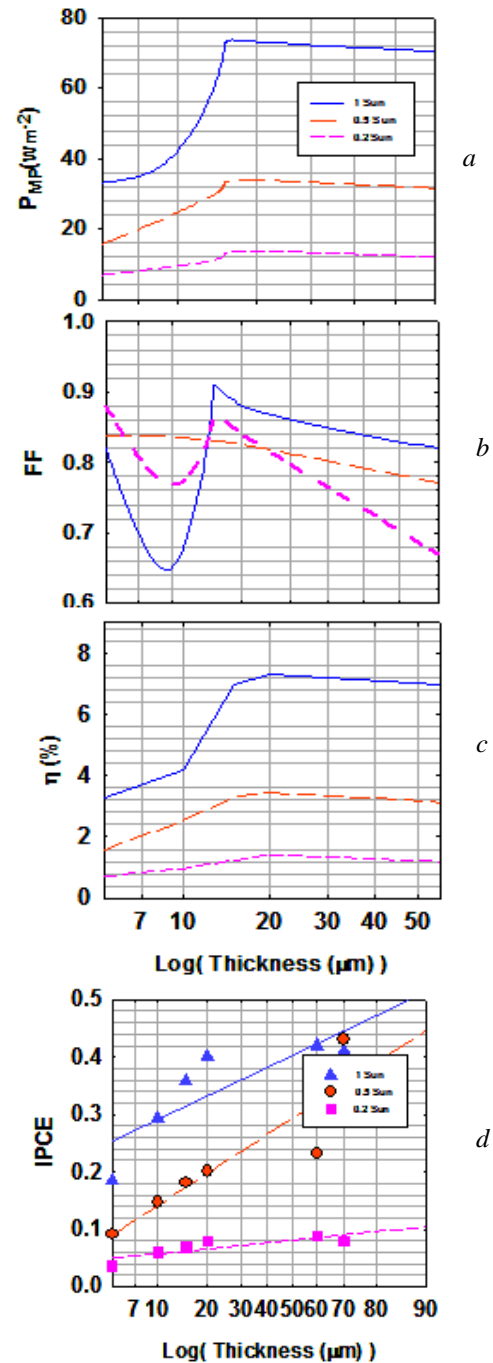


Fig. 11. The variations of P_{MP} (a), FF (b), η (c) and $IPCE$ (d) versus film thickness for different illumination intensities (d). The calculated data for $IPCE$ are linearly fitted to guide the eye.

4. Conclusion

A model based on multi-trap formalism and a standard electrochemical approach is implemented to simulate the transport properties of charged species involved in DSSC operation.

This model is capable of determining the effect of different performance parameters as well as cell features on the $J-V$ curve. The dependence of charged carrier densities, J_{SC} , V_{OC} , diffusion length and efficiency on film thickness, light intensity and direction were investigated. An efficiency limiting film thickness was calculated. The simulation shows fairly well the negative effect of TCO/electrolyte recombination current and recombination constant on V_{OC} . The presented modeling process can be used for an ad hoc fit to experimental data for a particular manufactured cell in order to find the parameters which control its performance. Further development of the present work for optimization of parameters involves introducing more fundamental parameters such as *LUMO-TiO₂CB* gap, the carrier hopping effect, and temperature and electron density dependent injection efficiency. Also, exploiting the model's potential to explain the recent improvement of the performance in cobalt-based electrolyte DSSCs is our future challenge.

References

- [1] B. O'Regan, M. Gratzel, *Nature* **353**, 737 (1991).
- [2] N. Memarian, I. Concina, A. Braga, S. M. Rozati, A. Vomiero, G. Sberveglieri, *Angew. Chem. Int. Ed.* **50**, 12321 (2011).
- [3] M. Adineh, P. Tahay, M. Ameri, N. Safari, E. Mohajerani, *RSC Adv.* **6**, 14512 (2016).
- [4] B. Yarmand, *J. Optoelectron. Adv. M.* **17**, 87 (2015).
- [5] H. Shahroosvand, P. Abbasi, M. Ameri, M. Riahi Dehkordi, *International Journal of Photoenergy* **2011**, (2011).
- [6] A. Yella, H. W. Lee, H. N. Tsao, C. Yi, A. K. Chandiran, M. K. Nazeeruddin, E. W. Diau, C. Y. Yeh, S. M. Zakeeruddin, M. Grätzel, *Science*, **334**, 629 (2011).
- [7] M. Ameri, F. Samavat, E. Mohajerani, M-R Fathollahi, *Journal of Physics D: Applied physics* **49**, 225601 (2016).
- [8] S. Salehi, M. Zamani, M. Ameri, *Journal of physics D: Applied Physics* **49**, 405601 (2016).
- [9] J. Ferber, J. Luther, R. Stangl, *Solar Energy Materials and Solar Cells* **53**, 29 (1998).
- [10] L. M. Peter, *Phys. Chem. Phys.* **9**, 2630 (2007).
- [11] M. Filipic, M. Berginc, F. Smole, M. Topic, *Current Applied Physics* **12**, 238 (2012).
- [12] T. Oda, S. Tanaka, S. Hayase, *Solar Energy Materials and Solar Cells* **90**, 2696 (2006).
- [13] J. A. Anta, F. Casanueva, G. Oskam, *J. Phys. Chem. B* **110**, 5372 (2006).
- [14] J. Villanueva, J. Anta, E. Guillen, G. Oskam, *J. Phys. Chem. C* **113**, 19722 (2009).
- [15] J. Villanueva, G. Oskam, J. A. Anta, *Solar Energy Materials and Solar Cells* **94**, 45 (2010).
- [16] K. Nithyanandam, R. Pitchumani, *Solar Energy* **86**, 351 (2012).
- [17] M. Ameri, F. Samavat, E. Mohajerani, *RSC Advances* **5**, 92690 (2015).
- [18] G. Franco, J. Gehring, L. M. Peter, E. A. Ponomarev, I. Uhlendorf, *J. Phys. Chem. B* **103**, 692 (1999).
- [19] D. Gentilini, A. Gagliardi, M. Auf der Maur, L. Vesce, D. D'Ercole, T. M. Brown, A. Reale, A. Di Carlo, *J. Phys. Chem. C* **116**, 1151 (2011).
- [20] J. A. Anta, J. Nelson, N. Quirke, *Phys. Rev. B* **65**, 125324 (2002).
- [21] J. Bisquert, V. S. Vikhrenko, *J. Phys. Chem. B* **108**, 2313 (2004).
- [22] M. K. Nazeeruddin, F. De Angelis, S. Fantacci, A. Selloni, G. Viscardi, P. Liska, S. Ito, B. Takeru, M. Grätzel, *J. Am. Chem. Soc.* **127**, 16835 (2005).
- [23] M. Ansari-Rad, Y. Abdi, E. Arzi, *J. Phys. Chem. C* **116**, 10867 (2012).
- [24] R. Memming, *Semiconductor Electrochemistry*, Weinheim, Wiley-VCH (2001).
- [25] T. Dittrich, *Phys Stat Sol (a)* **182**, 447 (2000).
- [26] K.-H. Jung, S.-R. Jang, R. Vittal, D. Kim, K.-J. Kim, *Bull. Korean Chem. Soc* **24**, 1501 (2003).
- [27] N.-G. Park, S. H. Chang, J. van de Lagemaat, K.-J. Kim, A. J. Frank, *Bull. Korean Chem. Soc.* **21**, 985 (2000).
- [28] M. K. Nazeeruddin, A. Podicio, I. Humphry-Baker, R. Müller, E. P. Liska, N. Vlachopoulos, M. Grätzel, *J. Am. Chem. Soc.* **115**, 6382 (1993).
- [29] E. Guillen, L. M. Peter, J. A. Anta, *Physical Chemistry Chemical Physics* **13**, 207 (2011).
- [30] M. Ansari-Rad, Y. Abdi, E. Arzi, *J. Appl. Phys.* **112**, 074319 (2012).
- [31] J. Krüger, R. Plass, M. Grätzel, Petra J. Cameron, L. M. Peter, *J. Phys. Chem. B* **107**, 7536 (2003).
- [32] L. M. Peter, K. G. U. Wijayantha, *Electrochemistry Communications* **1**, 576 (1999).
- [33] Young-Hun Kim, In-Kyu Lee, Yo-Seung Song, Myung-Hyun Lee, Bae-Yeon Kim, Nam-Ihn Cho, Deuk Yong Lee, *Electron. Mater. Lett.* **10**, 445 (2014).
- [34] Man Gu Kang, Kwang Sun Ryu, Soon Ho Chang, Nam Gyu Park, Jin Sup Hong, Kang-Jin Kim, *Bull. Korean Chem. Soc.* **25**, 742 (2004).
- [35] K. S. Ahn, M. Kang, J. K. Lee, B. C. Shin, J. W. Lee, *Applied Physics Letters* **89**, 013103 (2006).
- [36] S. Ito, Takuro N. Murakami, P. Comte, P. Liska, C. Grätzel, M. K. Nazeeruddin, M. Grätzel, *Thin Solid Films* **516**, 4613 (2008).
- [37] I. Shin, H. Seo, M. K. Son, K. Kim, J. K. Prabhakar, H. J. Kim, *Current applied physics* **10**, 422 (2010).
- [38] L.M. Peter, K.G.U. Wijayantha, *Electrochimica Acta* **45**, 4543 (2000).

*Corresponding author: m.ameri@basu.ac.ir